Rich Polymorphism of a Metal-Organic Framework in Pressure-Temperature Space

Journal:	*Journal of the American Chemical Society*
Manuscript ID	ja-2019-03234k.R1
Manuscript Type:	Article
Date Submitted by the Author:	16-May-2019
Complete List of Authors:	Widmer, Remo; University of Cambridge Department of Earth Sciences, Lampronti, Giulio; University of Cambridge, Earth Sciences Chibani, Siwar; Chimie ParisTech Wilson, Craig; Atomic Weapons Establishment Anzellini, Simone; Diamond Light Source Ltd Farsang, Stefan; University of Cambridge Department of Earth Sciences Kleppe, Annette; Diamond Light Source Ltd Casati, Nicola; Paul Scherrer Institut, Photon Science Division G. MacLeod, Simon; Atomic Weapons Establishment Redfern, Simon; University of Cambridge, Department of Earth Sciences Coudert, François-Xavier; PSL Research University, Chimie ParisTech – CNRS, Institut de Recherche de Chimie Paris Bennett, Thomas; University of Cambridge, Materials Science and Metallurgy

Rich Polymorphism of a Metal-Organic Framework in Pressure-Temperature Space

Remo N. Widmer[1], Giulio I. Lampronti[1], Siwar Chibani[2], Craig W. Wilson[3], Simone Anzellini[4], Stefan Farsang[1], Annette K. Kleppe[4], Nicola P. M. Casati[5], Simon G. MacLeod[3,6], Simon A. T. Redfern[1], François-Xavier Coudert[2] and Thomas D. Bennett[7]*

[1]Department of Earth Sciences, University of Cambridge, Downing Street, Cambridge CB2 3EQ, UK.

[2]Chimie ParisTech, PSL University, CNRS, Institut de Recherche de Chimie Paris, 75005 Paris, France.

[3]Atomic Weapons Establishment, Aldermaston, Reading, RG7 4PR, UK.

[4]Diamond Light Source Ltd, Harwell Science and Innovation Campus, Didcot, OX11 0DE, UK.

[5]Paul Scherrer Institute, Photon Science Division, WLGA/229 Forschungsstrasse 111, 5232 Villigen, Switzerland

[6]SUPA, School of Physics & Astronomy, and Centre for Science at Extreme Conditions, The University of Edinburgh, Edinburgh, EH9 3JZ, UK.

[7]Department of Materials Sciences & Metallurgy, University of Cambridge, 27 Charles Babbage Road, Cambridge CB3 0FS, UK.

Abstract

We present an *in-situ* powder X-ray diffraction study on the phase stability and polymorphism of the metal-organic framework ZIF-4, Zn(Imidazolate)$_2$, at simultaneous high-pressure and high-temperature, up to 8 GPa and 600 °C. The resulting pressure-temperature phase diagram reveals four, previously unknown, high-pressure-temperature ZIF phases. The crystal structures of two new phases – ZIF-4-cp-II and ZIF-hPT-II – were solved by powder diffraction methods. The total energy of ZIF-4-cp-II was evaluated using density functional theory calculations and was found to lie in between that of ZIF-4 and the most thermodynamically stable polymorph, ZIF-*zni*. ZIF-hPT-II was found to possess a doubly-interpenetrated diamondoid-topology and is isostructural with previously reported Cd(Imidazolate)$_2$ and Hg(Imidazolate)$_2$ phases. This phase exhibited extreme resistance to both temperature and pressure. The other two new phases could be assigned with a unit cell and space group, though their structures remain unknown. The pressure-temperature phase diagram of ZIF-4 is strikingly complicated when compared with that of the previously investigated, closely related ZIF-62, and demonstrates the ability to traverse complex energy landscapes of metal-organic systems using the combined application of pressure and temperature.

Introduction

Metal-organic frameworks (MOFs) are a subset of coordination polymers, consisting of three-dimensional, low-density networks of metal ions interlinked with organic ligands. Zeolitic imidazolate frameworks (ZIFs) are a sub-family of MOFs, populated by structures with tetrahedral metal nodes interconnected by ligands of imidazolate (Im, $C_3H_3N_2^-$) derivatives. The four-connected metal-N_4 building units of ZIFs show strong geometrical similarities with the four-connected SiO_4 and AlO_4 building units of inorganic zeolites, and therefore the two families share many network topologies[1]. Like zeolites, the ZIF family displays rich polymorphism, with variations in synthesis conditions alone yielding 18 polymorphs for the $Zn(Im)_2$ composition. These have distinct structures, densities, and topologies (Supplementary Table 1). Much computational[2] and experimental[3] effort has been expended in deducing the relative thermodynamic stabilities of these phases. Trends between structure and activity have also been established for mechanical[4] and thermal stability[5], structural flexibility[6], nitrogen[7] and hydrogen[8] adsorption, as well as mixed gas separation[9]. Among all those polymorphs, ZIF-4 with *cag* topology is relatively the most energetically stable[2], and most studied phase among the micro-porous $Zn(Im)_2$ compounds. ZIF-4 has a remarkable performance in separation of olefin/paraffin mixtures compared to other promising MOFs such as CPO-27 and MIL-53[10], the capability of adsorbing and retaining radioactive iodine[11], shaping abilities[12,13], and its synthesis is scalable[14], which demonstrates a potential for its industrial application. Meanwhile, ZIF-*zni* and ZIF-coi compete as the most stable dense polymorphs[15].

ZIF-4 also demonstrates diverse structural behavior at non-ambient conditions. On cooling, it undergoes a displacive phase transition to a structure of unchanged symmetry but with a strongly contracted unit cell volume[16]. On heating, ZIF-4 amorphizes above 250 °C. This amorphization event is characterized upon further heating by a transition from a low-density to a high-density glass[17]. The low-density state of ZIF-4 is particularly interesting because it may represent an amorphous state with a potential energy equivalent to the corresponding crystalline state. Such states have been termed 'perfect' glasses due to their relatively low entropy[18]. On further heating, the amorphous phase recrystallizes to a denser phase of *zni* topology (ZIF-*zni*) above 400 °C[19]. At 590 °C, ZIF-*zni* forms a quenchable melt of unaltered chemical composition and short-range order compared to its crystalline precursor[20]. ZIF-4 also undergoes significant structural changes under compression. A displacive phase transition to a denser phase at 0.03 GPa is followed by

amorphization around 1 GPa[21]. This amorphization is reversible upon decompression if the maximal reached pressure does not exceed a certain threshold pressure significantly[22].

The closely related ZIF-62 $Zn(Im)_{1.75}(bIm)_{0.25}$ (bIm: benzimidazolate, $C_7H_5N_2^-$) adopts the same topology and space group, and a similar unit cell to ZIF-4. However, approximately 12% of the imidazolate sites are instead occupied by benzimidazolate ligands. Our recent study of the pressure-temperature *(P-T)* phase diagram of ZIF-62 has demonstrated intriguing synergetic effects of the application of *P* and *T* on MOFs. For instance, the melting curve was shown to follow a negative Clapeyron slope, *i.e.* the melting temperature reduces with increasing pressure. Importantly, the simultaneous application of *P* and *T* has also been reported to play an important role in synthesizing materials with interesting physical properties. For example, the $TiCrO_3$ perovskite (containing strong covalent Ti–O bonds), synthesized at 6 GPa – 1230 °C, was shown to exhibit unusual magnetic properties[23]. Such methods can also be used to synthesize materials with unexpected chemical bonding, for example polymerized CO_2 with non-linear optical properties[24], and to industrially produce ultra-hard materials such as diamond and *c*-BN[25,26].

Motivated by the diverse response of ZIF-4 to application of either *P* or *T,* but the unknown consequence of simultaneous *P-T,* and as a complementary study to the phase diagram of ZIF-62, here we report the *P-T* behavior of ZIF-4 by means of *in-situ* synchrotron powder X-ray diffraction (PXRD) experiments in combination with a resistively-heated diamond anvil cell (DAC). The resultant *P-T* phase diagram demonstrates the formation and approximate stability range of new crystalline polymorphs of MOFs at high-*P-T* conditions. Overall this reflects a remarkably rich polymorphic system, especially when compared to the closely related ZIF-62 system.

Materials & Methods

Crystalline and fully evacuated ZIF-4 was prepared using previously established methods as described in the Supplementary Methods. The high-*P* experiment was performed at ambient temperature on the MS beamline (λ = 0.6200 Å) at the Swiss Light Source[27], Switzerland, using a membrane driven diamond anvil cell (MDAC) with Daphne Oil 7474 as a non-penetrating pressure transmitting medium. High-*P*-*T* experiments were performed on the I15 beamline (λ = 0.4246 Å) at Diamond Light Source, UK, using a resistively heated MDAC with silicone oil AP100 as a non-penetrating pressure transmitting medium. *In-situ* PXRD data were collected in a *P*-*T*-range from ambient pressure up to 8 GPa and from ambient temperature up to 580 °C. The temperature was measured with a K-type thermocouple attached close to one of the diamond anvils, while internal pressures were determined from the refined unit cell volumes of admixed NaCl and its equation-of-state parameters[28]. High-*T* PXRD data were collected under vacuum on a Bruker D8 Advance diffractometer equipped with a MRI radiation-heating stage (Physikalische Geräte GmbH, Germany). All heating- and pressure-increase rates as well as equilibration times are detailed in Supplementary Table 2. Structure solutions, and Rietveld and Lebail refinements were performed using the software package TOPAS-Academic V6[29]. Details on structure solution and refinement strategies can be found in the Supplementary Methods, alongside the observed diffraction data.

Periodic density functional theory (DFT) calculations were performed with the Vienna Ab initio Simulation Package (VASP)[30–32]. The electron–ion interactions were described using the projector-augmented wave (PAW) method developed by Blöchl[33]. The Kohn-Sham equations were solved self-consistently until the energy was converged within 10^{-6} eV. The semilocal PBE exchange-correlation functional was employed[34]. However, this level of theory is known to lack the correct description of long-range dispersion interactions[35], and in the present work we used the PBE-D3 scheme for correction of dispersion interactions, which was shown to provide a good description of MOF structures[36]. The plane wave cutoff energy was set to 550 eV and partial orbital occupancies were smeared using the Gaussian smearing scheme[37] with a smearing parameter σ = 0.2 eV. The relaxation of the structures was performed until all forces acting on the atoms were smaller than 0.03 eV/Å. Due to the large unit cell sizes considered, the Brillouin-zone sampling was restricted to the Γ-point.

Results and Discussion

ZIF-4 at high-*P* – ambient-*T*

The high-*P* behavior at ambient-*T* of ZIF-4 has previously been studied under a variety of conditions. The findings of previous studies[21,22] and our own results alongside indication of the respective experimental conditions, are shown in Figure 1. A summary of crystal structural parameters of all high-*P* – ambient-*T* phases of ZIF-4 is given in Table 1. PXRD patterns are shown in Supplementary Figure 1. Representative whole-pattern fitting results to experimental PXRD data are given in Supplementary Figure 2.

Two previous studies reported two distinct, monoclinic, high-*P* phases of ZIF-4: ZIF-4-I in the presence of solvent, and ZIF-4-cp for the evacuated framework[21,22]. Here, we found a rapid transformation of ZIF-4 at pressure below 0.1 GPa to an unreported orthorhombic phase, which is termed ZIF-4-cp-II (closed pore), in accordance with the established nomenclature. ZIF-4 and ZIF-4-cp-II coexist over a range of approximately 0.5 GPa. We did not observe amorphization of the denser polymorph above 1 GPa, in contrast to the other two high-*P* phases reported in previous studies. Instead we observed a further transformation of ZIF-4-cp-II to another unreported phase, which is termed ZIF-4-cp-III. This new form is characterized by a symmetry lowering to a monoclinic system, which results in the appearance of new diffraction peaks. ZIF-4-cp-III only amorphizes above 7 GPa.

Though these results may appear to conflict with previous studies, the pressure increase rate (PIR) is vastly different. During the experiment reported here, the pressure was deliberately increased at a high rate of approximately 2.5 GPa/minute up to 8 GPa, which is an estimated 100 times faster than achievable in conventional experiments as reported in previous experiments[21,22]. As has been observed in pressure-mediated transitions of other solid state materials,[38] this higher PIR facilitates a richer range of polymorphic behavior than witnessed in other studies. This effect is the result of a non-equilibrium transformation process induced by the substantially higher PIR. As a result, the formation of ZIF-4-cp-II preempts the formation of ZIF-4-cp and the formation of ZIF-4-cp-III preempts the formation of *a*-ZIF-4. It thus becomes apparent that the kinetic control of the pressurization rate plays an important role, though this is rarely taken into consideration[38].

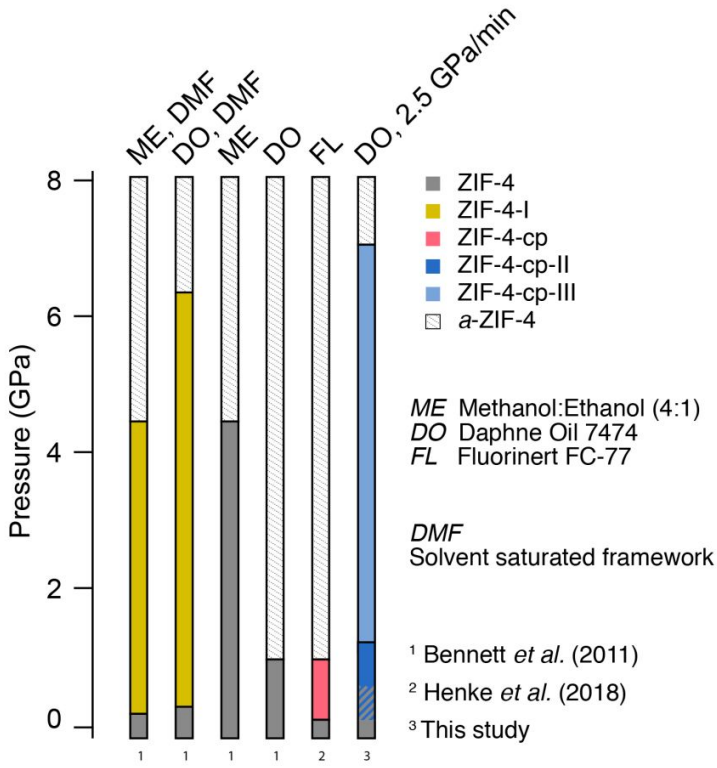

Figure 1. *Phase domains of ZIF-4 as reported in several high-P experiments performed at ambient-T using different pressure transmitting media and pressure increase rates. The hatched region on the last column (3) indicates an overlap of two adjacent phases.*

Table 1. *Lattice parameters of the high-pressure – ambient-temperature polymorphs of ZIF-4 as measured at the reported pressure and temperature.*

	ZIF-4	**ZIF-4-I**	**ZIF-4-cp**	**ZIF-4-cp-II**	**ZIF-4-cp-III**
a (Å)	15.395	17.608	14.235	14.506	15.828
b (Å)	15.307	14.411	14.874	14.313	14.211
c (Å)	18.426	14.703	16.33	14.714	14.266
ß (°)	90	100.90	91.55	90	116.13
Vol (Å^3)	4342	3664	3457	3055	2882
Space Group	*Pbca*	*P2$_1$/c*	*P2$_1$/c*	*Pbca*	*P2$_1$/c*
P (GPa)	0	0	0.08	0.65	1.48
T (°C)	25	25	25	25	25
CSD/CCDC	VEJYU	VEJYUF0	n.a.	1903482	n.a.
Ref.	[7]	[22]	[21]	This study	This study

ZIF-4 at high-*P* – high-*T*

The *P*-*T*-diagram shown in Figure 2 contains the traces of four individual runs of simultaneous *P* and *T* increase, and one trace each of the high-*P* – ambient-*T,* and the ambient-*P* – high-*T* runs. PXRD patterns are shown in Supplementary Figure 3-7. Representative whole-pattern fits for all phases are given in Supplementary Figure 8 and 9. The phases observed at each *P*-*T* point are represented by the color of the markers, and schematic phase boundaries are indicated by colored fields, strictly as a guide to the eye only. Transitions, which occur via reconstructive processes, *i.e.* Zn-N bond breaking, are indicated by dashed lines. The simultaneous application of *P* and *T* to ZIF-4 resulted in the formation of two novel polymorphs, in addition to the two high-*P*-ambient-*T* phases discussed earlier, and the known amorphous *a*-ZIF-4, the recrystallized ZIF-*zni,* and liquid ZIF-4. Table 2 details the crystal structural parameters of the high-*P*-*T* phases. The first transition at simultaneous high-*P*-*T* is that of ZIF-4 / ZIF-4-cp-II, which occurs just below 40 °C and 0.1 GPa. This transition is the same as that at high-*P* – ambient-*T*, which was discussed in the previous section. In contrast to the ambient-*T* experiment, the simultaneous application of heat here stabilizes the ZIF-4-cp-II phase up to at least 8 GPa and 250 °C, without further transition to ZIF-4-cp-III. However, at comparatively lower pressures but higher temperatures (140 °C – 4 GPa, and 250 °C – 2.6 GPa), ZIF-4-cp-II amorphizes to *a*-ZIF-4. This is analogous to the amorphization of ZIF-4 to *a*-ZIF-4 at 250 °C – ambient-*P*[39] and the at 170 °C – 0.075 GPa. Importantly, the Clapeyron slope of the ZIF-4 – *a*-ZIF-4 transformation is negative, while that of the ZIF-4-cp-II – *a*-ZIF-4 transformation is positive. This implies increasing relative densities in the order ZIF-4 < *a*-ZIF-4 < ZIF-4-cp-II. An equivalent change of the slope from negative to positive with increasing *P* has been reported for the melting curve of ZIF-62[40]. Upon further heating and pressurization of *a*-ZIF-4, two new transformations are associated with the recrystallization of two distinct high-*P*-*T* phases: ZIF-hPT-I at 0.4 GPa – 270 °C, and ZIF-hPT-II at 0.8 GPa – 290 °C and 3 GPa – 320 °C. Both new phases, ZIF-hPT-I and ZIF-hPT-II remain stable until the maximal achieved *P*-*T* conditions of these experiments. Importantly, we did not observe the melting of these phases within the given temperature limits. The melting curve of ZIF-*zni* at elevated *P* is thus tentatively indicated with a positive Clapeyron slope. We justify this behavior by the formation of the high-density crystalline phases ZIF-hPT-I and ZIF-hPT-II prior to the (hypothetical) melting. In contrast, the previously reported melting behavior of ZIF-62 follows a negative Clapeyron slope due to the higher density of the liquid compared to the solid-amorphous precursor.

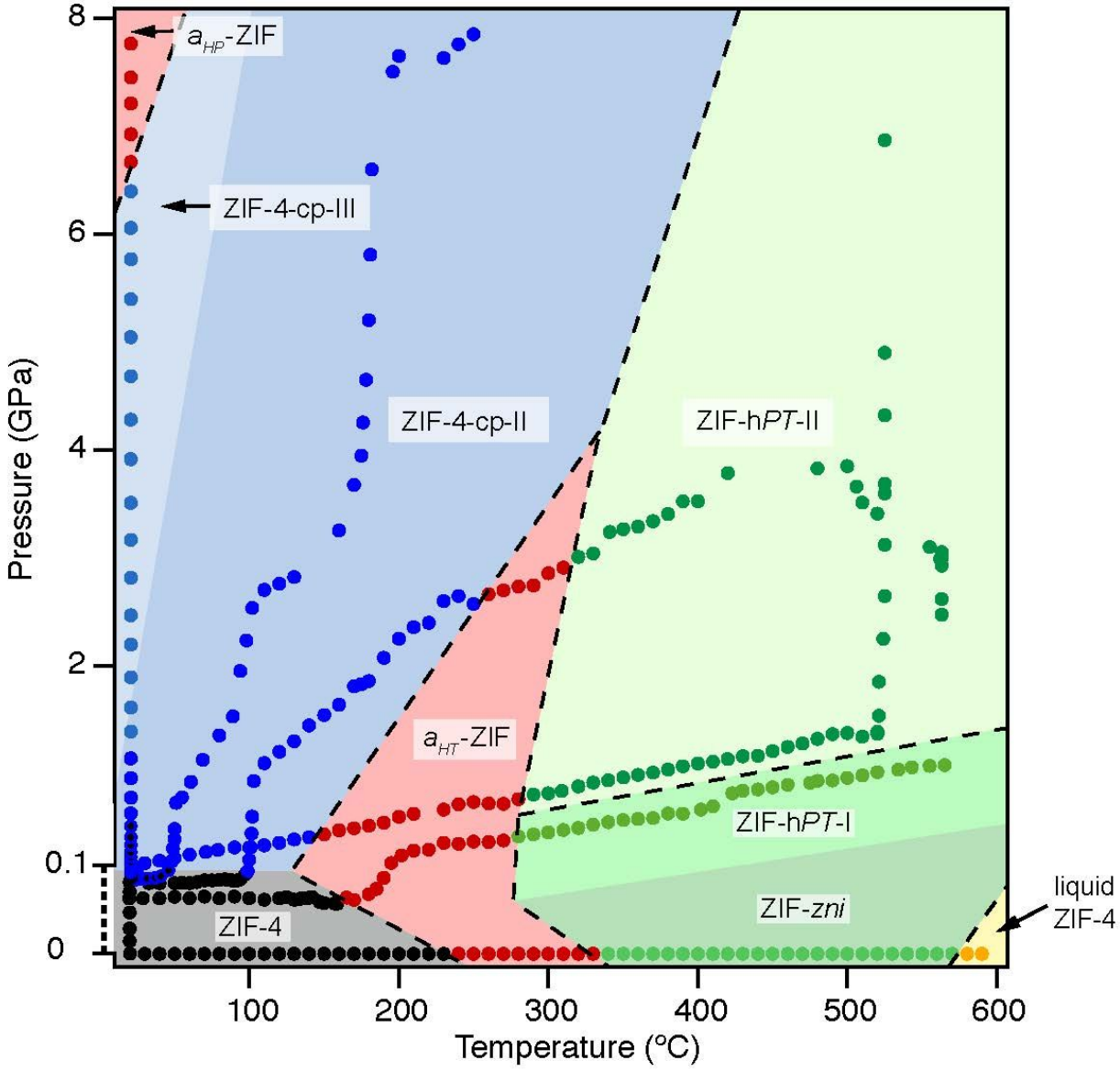

Figure 2. *Pressure-temperature phase diagram of ZIF-4. The pressure-range from 0 GPa to 0.1 GPa has been magnified for better visibility and is thus not to scale. Solid symbols represent the experimental points and they are colored according to the phases observed in-situ. Colored outlines of phase boundaries are drawn as guides to the eye. Dashed lines indicate irreversible, reconstructive transitions.*

Table 2. *Lattice parameters of the high-pressure – high-temperature polymorphs of ZIF-4 as measured at the reported pressure and temperature.*

	ZIF-cp-II	**ZIF-*zni****	**β-ZIF-*zni*[#]**	**ZIF-hPT-I***	**ZIF-hPT-II***
*a (*Å)	15.386	23.481	22.748	22.863	9.557
*b (*Å)	14.336	23.481	22.748	23.839	10.100
*c (*Å)	14.740	12.461	13.017	11.636	14.099
Vol (Å^3)	3251	6871	6736	6342	1361
Space Group	*Pbca*	*$I4_1cd$*	*$I4_1$*	n.a.[†]	*Pbca*
Topology	cag	*zni*	*zni*	n.a.	double-dia
P (GPa)	0.15	0	0	0.46	0.81
T (°C)	30	25	25	300	290
CSD/CCDC	xxx	IMIDZB	IMIDZB12	n.a.	1903495
Ref.	This work	[41]	[42]	This work	This work

* recrystallized from amorphous a-ZIF-4.

[#] high-pressure form of ZIF-*zni*, not observed during our experiments.

[†] the space group has not unequivocally been determined - a space group with no systematic absences (*Pmmm*) was used for the Pawley refinement.

Crystal structures

ZIF-4-cp-II

The unit cell and space group for ZIF-4-cp-II were found to be identical with those of the ZIF-4-LT structure, which occurs when ZIF-4 is cooled below -130 °C[16]. Based on the ZIF-4-LT model, we successfully refined a structural model for ZIF-cp-II (Supplementary Methods). The difference between ZIF-4 and the new high-*P* ZIF-4-cp-II phase, both orthorhombic with space group *Pbca*, is a density increase by a factor of approximately 1.35, which is marked by an abrupt volume contraction (Supplementary Figure 10). This densification is accomplished by a displacive transition (*i.e.* a rearrangement without breaking bonds) involving the rotation of the imidazolate linkers around the N–N hinge, and the increase of Zn–Im–Zn angles by (on average) 10°. While the topology is preserved upon this densification, the 6- and 8-membered rings of the cag topology are visibly squeezed (Figure 3). A similar mechanism was described for the ZIF-4 – ZIF-4-LT transformation[16]. An overlay of the asymmetric units of ZIF-cp-II and ZIF-4-LT is shown Supplementary Figure 11.

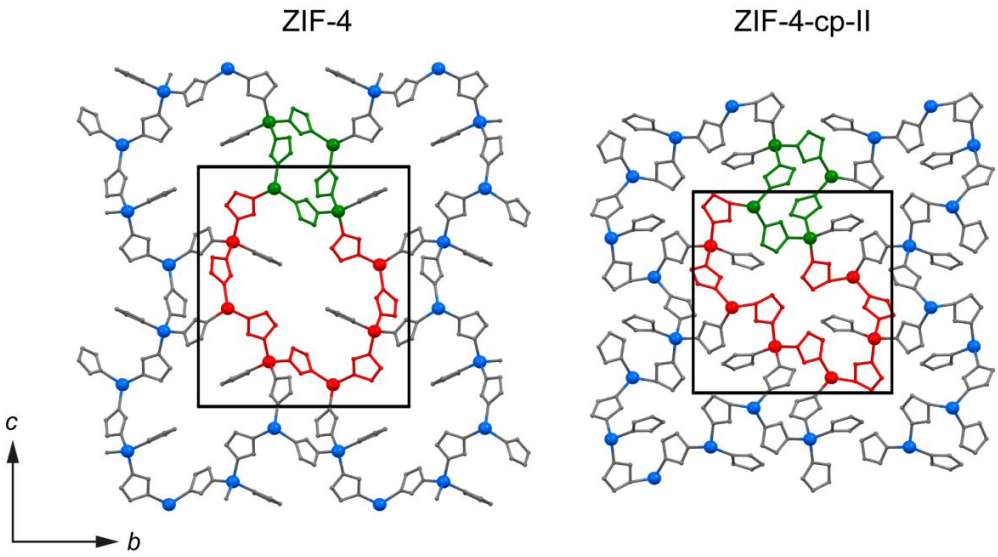

Figure 3. *Comparison of the structures of ZIF-4 (left) and ZIF-4-cp-II at 0.2 GPa (right). Zn = blue, imidazolate = grey, H is omitted. The 4-, and 8-membered rings of the cag topology are indicated in green and red, respectively.*

ZIF-4-cp-III

The structure of ZIF-4-cp-III could not be reliably determined due to poor data quality. However, since the transition from ZIF-4-cp-II to ZIF-4-cp-III is instantaneous, we suggest that this orthorhombic to monoclinic transition can be classified as a displacive transition, and that the structure retains the cag topology. The unit cell volume continuously decreases across the ZIF-4-cp-II – ZIF-4-cp-III transition (Supplementary Figure 10).

ZIF-hPT-I

The structure of ZIF-hPT-I could not be solved based on the present data. However, we propose a unit cell based on successful structure-less refinements (Table 2). Consequently, it is unclear to what extend ZIF-hPT-I structurally differs from ZIF-*zni*, and its high-*P* polymorph β-ZIF-*zni*, given the very similar unit cell dimensions of all three phases (Table 2). Furthermore, interconversion of the two phases ZIF-hPT-I and ZIF-hPT-II, is kinetically hindered, as demonstrated by their widely overlapping apparent stabilities (Supplementary Figure 12). The most likely explanation for these meta-stable extensions is a distinct topology of the two structures. This would imply that any transition between them is reconstructive, *i.e.* requires the

breakage and reformation of Zn–N bonds for interconversion. Further evidence for a distinct topology stems from the observation that around 550 °C ZIF-hPT-I amorphized at 6 GPa, while ZIF-hPT-II proofed stable at least up to 8 GPa (Supplementary Figure 12).

ZIF-hPT-II

The structure of ZIF-hPT-II (Figure 4) was found to be isostructural to previously reported $Cd(Im)_2$ and $Hg(Im)_2$ phases[43] and is based on a double-interpenetrated diamondoid network. This interpenetration is surprising given the relative short Zn–N bonds compared to Cd–N and Hg–N bonds, and previously it had therefore been deemed impossible for a $Zn(Im)_2$ compound[43]. Twofold interpenetrated diamondoid $Zn(Im)_2$ networks have also been simulated in a number of space groups, none of which was found to be energetically favorable at ambient conditions[44]. Whether ZIF-hPT-II is stable at ambient conditions remains experimentally unknown, though it is unlikely to undergo a reconstructive bond breaking process upon decompression.

A second-order Birch-Murnaghan equation of state was fitted from 1.4 to 4.9 GPa to the refined unit cell volumes of ZIF-hPT-II using EOSfit7-GUI[45], obtained from isothermal compression at 520 °C. The resulting bulk modulus (K_0) is 21.6(1) GPa (Supplementary Figure 13). In comparison, the dense ZIF-*zni* has a bulk modulus of approximately 14 GPa at ambient temperature[42].

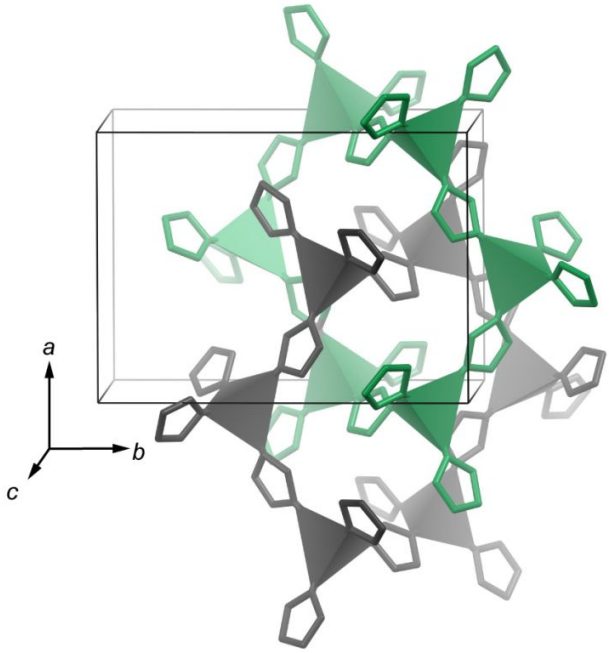

Figure 4. *Structural model of ZIF-hPT-II represented by ZnN_4 tetrahedra and imidazolate linkers without H atoms (unit cell content is reduced for clarity). Two interpenetrated, unconnected diamondoid networks in grey and green emerge based on the interconnected $Zn(Im)_4$ units.*

DFT calculations

Energy minimization calculations were performed for ZIF-4-cp-II, ZIF-4, and ZIF-*zni* in order to validate the energetic stability of the new, experimentally determined high-*P* polymorph ZIF-4-cp-II

Table 3). The lattice parameters of the conventional cell are given in Supplementary Table 3. The absolute energies calculated here for ZIF-4 and ZIF-*zni* are slightly higher compared to those resulting from similar calculations, which is in line with the fact that previous calculations

were performed without dispersion correction[2]. Interestingly, the energy of ZIF-4-cp-II is intermediate to those of ZIF-4 and ZIF-*zni*, despite being the densest structure amongst the three. This, and the observation that relaxing its unit cell leads to an expansion, points out that the structure is highly strained, and only accessible under high-*P* conditions.

Table 3. *Calculated densities and energies of ZIF-4-cp-II and ZIF-4 per Zn atom, relative to ZIF-zni, for fixed and relaxed unit cells.*

	ZIF-*zni*		**ZIF-4-cp-II**		**ZIF-4**	
	($g.cm^{-3}$)	(kJ/mol)	($g.cm^{-3}$)	(kJ/mol)	($g.cm^{-3}$)	(kJ/mol)
Fixed unit cell	1.468	0	1.630	+148.54	1.210	+210.54
Relaxed unit cell	1.546	0	1.575	+204.67	1.246	+224.07

Comparison of ZIF-4 and ZIF-62 at high-*P-T* conditions

It is well known how ZIF-4 and its partially linker substituted relative ZIF-62 substantially differ in their high-*T* behavior[20]. For example, the recrystallization mechanism leading to the transformation of ZIF-4 to ZIF-*zni* upon heating is inhibited in ZIF-62 due to the presence of bulky bIm ligands. The presence of bIm also lowers the melting temperature of ZIF-62 relative to ZIF-4 and extends the stability range of that melt. Comparison of the high-*P-T* behavior of ZIF-4 with that of ZIF-62 reveals an even wider-ranging control of the presence of the bIm linker. In fact, none of the displacive or reconstructive transformations at high-*P-T* conditions observed in ZIF-4 occur in ZIF-62. Meanwhile, ZIF-62 amorphizes above 5 GPa, while ZIF-4 has been shown to undergo *P*-induced amorphization at comparable pressurization rates at a much lower *P* of around 1 GPa[22]. The significant difference in high-*P* stability at ambient-*T* between these two ZIFs may, again, be explained by the more sterically hindered bIm linkers protruding into the pore cavities and offering additional stabilization against collapse. This structural stabilization of ZIF-62 through linker substitution has been confirmed by force-field based molecular dynamics simulations of the elastic properties of ZIF-62 and ZIF-4[40]. Furthermore, in the case of ZIF-62, we inferred the existence of distinct, though adjacent, high-*T* and high-*P* amorphous phases[40]. Here, in the case of ZIF-4, the two equivalent high-*T* and high-*P* amorphous phases are separated by other crystalline phases. This is further support that the high-

T and high-*P* induced amorphous phases of this ZIF system, as previously reported, indeed are structurally distinct.

Critical considerations

The compilation of all the high-*T*, high-*P* and high-*P*-*T* polymorphs reported in previous literature and the present study into a single thermodynamically valid *P*-*T* phase-diagram requires critical consideration of several experimental and theoretical issues: (1) the rates of pressure- and temperature increase, (2) the influence of the pressure transmitting media, (3) sample dependent effects (4) the definition of a phase transition, and (5) whether the overall energy landscape of the system with $Zn(Im)_2$ composition, or the local energy landscape of the ZIF-4 network with cag topology is in question.

(1) Experimentally determined phase boundaries will always depend on the transformation kinetics between the two adjacent phases. In particular, reconstructive transformations can be very sluggish and may allow a phase to persist in a meta-stable state beyond its thermodynamic *P*-*T* stability field[46]. Furthermore, kinetic effects can allow two distinct phases to coexist over a certain range of conditions. The single most important factor here is the applied pressurization and/or heating rate. In addition to the shifting of apparent phase boundaries, there is also a possibility that altogether different polymorphs form depending on these rates[38].

(2) Different types of non-penetrating pressure transmitting media have been used in past and present studies. Fluorinert, silicone oil, and Daphne Oil have distinct hydrostatic limits at ambient temperature of approximately 2 GPa, 2.5 GPa, and 4 GPa, respectively[47]. This limit will affect the on-set pressures of amorphization[48,49], and may therefore also preclude the transformation to higher-pressure polymorphs. Furthermore, it appears that the type of pressure transmitting medium also affects the structure of high-*P* polymorphs. Upon pressurizing ZIF-4 at ambient-*T*, the use of Fluorinert affords the monoclinic ZIF-4-cp, while both the use of Daphne Oil and silicone oil result in the orthorhombic ZIF-4-

cp-II. This can only be explained by an unknown and unexpected interaction of the medium with ZIF-4.

(3) There are several sample dependent factors which have been shown to influence the experimental outcome of non-ambient studies. For example, residual solvent molecules in microporous materials has been shown to inhibit[16] as well as promote[22] phase transitions. It is therefore important to either carefully evacuation, or deliberately solvate starting materials. Furthermore, it is widely accepted that crystallite size can play a major role and affect the thermodynamic landscape of phase transitions[50,51]. However, such effects only become significant when the crystal size is decreased to the nm scales[52].

(4) Additional difficulties for determining accurate phase boundaries arise from the softness[53] of porous structures. Depending on the available data, it is not always a clear-cut distinction whether the response to variable pressure or temperature is that of a phase transition *sensu stricto,* or that of a highly flexible structure accommodating a large degree of continuous geometric relaxation. For instance, the low-temperature transition in ZIF-4 was structurally described as a symmetry preserving continuous volume contraction[16]. Yet it classifies as a discontinuous phase transition given an exothermic signal found in differential scanning calorimetry measurements. A combination of techniques may therefore be necessary to clearly detect and identify phase boundaries.

(5) Finally, the interpretation of experimentally derived *P-T-p*hase diagrams of porous coordination polymers requires a clear definition of the scope of phase-stability. High kinetic barriers can extend the apparent stability of some phases indefinitely, or prevent the formation of certain phases altogether, as discussed in point (1). This is exemplified very well indeed by the behavior of ZIF-4. The intricate network of ZIF-4 is difficult to recrystallize, *i.e.* transform reconstructively, due to bulky and rigid organic molecules. As a result, ZIF-4 is metastable up to approximately 250 °C[3]. Above this temperature, instead of transforming to the most stable crystalline conformation, the system adopts an energetically intermediate amorphous state[39,48]. At higher temperature still, when a

reconstructive transition is kinetically possible, ZIF-4 recrystallizes to ZIF-*zni*. However, ZIF-*zni* only represents the thermodynamically stable phase above 360 °C, despite the fact that it is recoverable to ambient conditions[15]. The thermodynamically most stable phase between ambient-*T* and the formation of ZIF-*zni*, ZIF-*coi*[15], was never observed — which might be attributed to it lying very close in density and energy to ZIF-*zni*. As a consequence of these kinetic controls, the outcome of a *P*-*T* phase diagram study in strongly associated systems like MOFs will strongly depend on the *P*-*T* paths taken during the experiment.

With regard to the *P*-*T* diagrams of ZIF-4 here, it is, for example, unclear whether the transformation of ZIF-4 to the iso-topological ZIF-4-cp-III reflects a global energy minimization. The known competing phase, β-ZIF-*zni*, has an almost identical density, and a potential high-*P* polymorph of ZIF-coi is also likely to exist, but has not yet been described. Furthermore, the onsets of crystallizations of the ZIF-hPT-I and ZIF-hPT-II phases are unlikely to reflect a transition dictated only by a favorable change in free energy. It is more likely that these transitions mark the overcoming of thermal activation barriers for recrystallization. In conclusion, the phase diagrams presented here are technically not thermodynamic phase diagrams *sensu stricto*, but indications of phase behavior under a certain set of conditions.

Conclusions

We have investigated the phase stability ZIF-4 at simultaneous high-*P* and high-*T* using *in-situ* powder X-ray diffraction. The relatively narrow stability field of ZIF-4 extends up to approximately 0.1 GPa and 250 °C. The subsequent structural changes observed at higher *P*-*T* conditions can be grouped into the two categories of displacive and reconstructive transformations. The closed-pore phases ZIF-4-cp, ZIF-4-cp-II and ZIF-4-cp-III, which border ZIF-4, preserve the chemical bonding and thus the underlying cag topology upon transition. Separated from ZIF-4 by an amorphous field, the high-*P*-*T* phases ZIF-*zni*, ZIF-hPT-I, and ZIF-

hPT-II represent entirely recrystallized structures with new topologies, which are the first high *P-T* crystalline MOF polymorphs observed. This bodes well for the continued exploration of the high-*P-T* materials space. Altogether, these dense $Zn(Im)_2$ polymorphs span a large stability range in *P-T* space up to at least 8 GPa and 580 °C – a considerable scope for a compound containing organic molecules.

Associated Content

Supporting Information

The Supporting Information is available free of charge on the ACS Publications website: Experimental details, simulation results, PXRD patterns, Rietveld fits, and crystal-structural details.

Author Information

Corresponding Author

*tdb35@cam.ac.uk

Acknowledgments

R.N.W. acknowledges support from the EPSRC in the form of a DTG Graduate Studentship. T.D.B. thanks the Royal Society for a University Research Fellowship and for their support (UF150021). Access to HPC platforms was provided by a GENCI grant (A0050807069). We thank Diamond Light Source for access to beamline I15 (EE19046-1) and Swiss Light Source for access to MS-powder beamline (20180882).

References

(1) Eddaoudi, M.;Sava, D. F.;Eubank, J. F.;Adil, K.;Guillerm, V. Zeolite-like Metal-Organic Frameworks (ZMOFs): Design, Synthesis, and Properties. *Chem. Soc. Rev.* **2015**, *44*, 228–249.

(2) Lewis, D. W.;Ruiz-Salvador, A. R.;Gomez, A.;Rodriguez-Albelo, L. M.;Coudert, F.-X.;Slater, B.;Cheetham, A. K.;Mellot-Draznieks, C. Zeolitic Imidazole Frameworks: Structural and Energetics Trends Compared with Their Zeolite Analogues. *CrystEngComm* **2009**, *11*, 2272–2276.

(3) Hughes, J. T.;Bennett, T. D.;Cheetham, A. K.;Navrotsky, A. Thermochemistry of Zeolitic Imidazolate Frameworks of Varying Porosity. *J Am Chem Soc* **2013**, *135*, 598–601.

(4) Tan, J. C.;Bennett, T. D.;Cheetham, A. K. Chemical Structure, Network Topology, and Porosity Effects on the Mechanical Properties of Zeolitic Imidazolate Frameworks. *Proc Natl Acad Sci U S A* **2010**, *107*, 9938–9943.

(5) Bouëssel Du Bourg, L.;Ortiz, A. U.;Boutin, A.;Coudert, F. X. Thermal and Mechanical Stability of Zeolitic Imidazolate Frameworks Polymorphs. *APL Mater.* **2014**, *2*, 124110–124118.

(6) Gao, M.;Misquitta, A. J.;H. N. Rimmer, L.;Dove, M. T. Molecular Dynamics Simulation Study of Various Zeolitic Imidazolate Framework Structures. *Dalt. Trans.* **2016**, *45*, 4289–4302.

(7) Park, K. S.;Ni, Z.;Côté, A. P.;Choi, J. Y.;Huang, R.;Uribe-Romo, F. J.;Chae, H. K.;O'Keeffe, M.;Yaghi, O. M. Exceptional Chemical and Thermal Stability of Zeolitic Imidazolate Frameworks. *Proc. Natl. Acad. Sci.* **2006**, *103*, 10186–10191.

(8) Chen, E.-Y.;Liu, Y.-C.;Zhou, M.;Zhang, L.;Wang, Q. Effects of Structure on Hydrogen Adsorption in Zeolitic Imidazolate Frameworks. *Chem. Eng. Sci.* **2012**, *71*, 178–184.

(9) Battisti, A.;Taioli, S.;Garberoglio, G. Zeolitic Imidazolate Frameworks for Separation of Binary Mixtures of CO_2, CH_4, N_2 and H_2: A Computer Simulation Investigation. *Microporous Mesoporous Mater.* **2011**, *143*, 46–53.

(10) Hartmann, M.;Böhme, U.;Hovestadt, M.;Paula, C. Adsorptive Separation of Olefin/Paraffin Mixtures with ZIF-4. *Langmuir* **2015**, *31*, 12382–12389.

(11) Bennett, T. D.;Saines, P. J.;Keen, D. A.;Tan, J.-C.;Cheetham, A. K. Ball-Milling-Induced Amorphization of Zeolitic Imidazolate Frameworks (ZIFs) for the Irreversible Trapping of Iodine. *Chem. – A Eur. J.* **2013**, *19*, 7049–7055.

(12) Tian, T.;Velazquez-Garcia, J.;Bennett, T. D.;Fairen-Jimenez, D. Mechanically and Chemically Robust ZIF-8 Monoliths with High Volumetric Adsorption Capacity. *J. Mater. Chem. A* **2015**, *3*, 2999–3005.

(13) Widmer, R. N.;Lampronti, G. I.;Kunz, B.;Battaglia, C.;Shepherd, J. H.;Redfern, S. A. T.;Bennett, T. D. Manufacturing Macroporous Monoliths of Microporous Metal–Organic Frameworks. *ACS Appl. Nano Mater.* **2018**, *1*, 497–500.

(14) Hovestadt, M.;Vargas Schmitz, J.;Weissenberger, T.;Reif, F.;Kaspereit, M.;Schwieger, W.;Hartmann, M. Scale-up of the Synthesis of Zeolitic Imidazolate Framework ZIF-4. *Chemie-Ingenieur-Technik* **2017**, *89*, 1374–1378.

(15) Schröder, C. A.;Baburin, I. A.;van Wüllen, L.;Wiebcke, M.;Leoni, S. Subtle Polymorphism of Zinc Imidazolate Frameworks: Temperature-Dependent Ground States in the Energy Landscape Revealed by Experiment and Theory. *CrystEngComm* **2013**, *15*, 4036–4040.

(16) Wharmby, M. T.;Henke, S.;Bennett, T. D.;Bajpe, S. R.;Schwedler, I.;Thompson, S.

P.;Gozzo, F.;Simoncic, P.;Mellot-Draznieks, C.;Tao, H.;Yue, Y.;Cheetham, A. K. Extreme Flexibility in a Zeolitic Imidazolate Framework: Porous to Dense Phase Transition in Desolvated ZIF-4. *Angew. Chemie Int. Ed.* **2015**, *54*, 6447–6451.

(17) Bennett, T. D.;Tan, J.-C.;Yue, Y.;Baxter, E.;Ducati, C.;Terrill, N. J.;Yeung, H. H. M.;Zhou, Z.;Chen, W.;Henke, S.;Cheetham, A. K.;Greaves, G. N. Hybrid Glasses from Strong and Fragile Metal-Organic Framework Liquids. *Nat. Commun.* **2015**, *6*, 8079–8086.

(18) Angell, C. A.;Moynihan, C. T.;Hemmati, M. `Strong' and `superstrong' Liquids, and an Approach to the Perfect Glass State via Phase Transition. *J. Non. Cryst. Solids* **2000**, *274*, 319–331.

(19) Bennett, T. D.;Goodwin, A. L.;Dove, M. T.;Keen, D. A.;Tucker, M. G.;Barney, E. R.;Soper, A. K.;Bithell, E. G.;Tan, J.-C.;Cheetham, A. K. Structure and Properties of an Amorphous Metal-Organic Framework. *Phys. Rev. Lett.* **2010**, *104*, 115503.

(20) Bennett, T. D.;Yue, Y.;Li, P.;Qiao, A.;Tao, H.;Greaves, N. G.;Richards, T.;Lampronti, G. I.;Redfern, S. A. T.;Blanc, F.;Farha, O. K.;Hupp, J. T.;Cheetham, A. K.;Keen, D. A. Melt-Quenched Glasses of Metal–Organic Frameworks. *J. Am. Chem. Soc.* **2016**, *138*, 3484–3492.

(21) Henke, S.;Wharmby, M. T.;Kieslich, G.;Hante, I.;Schneemann, A.;Wu, Y.;Daisenberger, D.;Cheetham, A. K. Pore Closure in Zeolitic Imidazolate Frameworks under Mechanical Pressure. *Chem. Sci.* **2018**, *9*, 1654–1660.

(22) Bennett, T. D.;Simoncic, P.;Moggach, S. A.;Gozzo, F.;Macchi, P.;Keen, D. A.;Tan, J.-C.;Cheetham, A. K. Reversible Pressure-Induced Amorphization of a Zeolitic Imidazolate Framework (ZIF-4). *Chem. Commun.* **2011**, *47*, 7983–7985.

(23) Yi, W.;Matsushita, Y.;Katsuya, Y.;Yamaura, K.;Tsujimoto, Y.;Presniakov, I. A.;Sobolev, A. V;Glazkova, Y. S.;Lekina, Y. O.;Tsujii, N.;Nimori, S.;Takehana, K.;Imanaka, Y.;Belik, A. A. High-Pressure Synthesis, Crystal Structure and Magnetic Properties of $TlCrO_3$ Perovskite. *Dalt. Trans.* **2015**, *44*, 10785–10794.

(24) Iota, V.;Yoo, C. S.;Cynn, H. Quartzlike Carbon Dioxide: An Optically Nonlinear Extended Solid at High Pressures and Temperatures. *Science* **1999**, *283*, 1510–1513.

(25) Kurdyumov, A. V;Britun, V. F.;Petrusha, I. A. Structural Mechanisms of Rhombohedral BN Transformations into Diamond-like Phases. *Diam. Relat. Mater.* **1996**, *5*, 1229–1235.

(26) Bovenkerk, H. P.;Bundy, F. P.;Hall, H. T.;Strong, H. M.;Wentorf, R. H. Preparation of Diamond. *Nature* **1959**, *184*, 1094–1098.

(27) Willmott, P. R.;Meister, D.;Leake, S. J.;Lange, M.;Bergamaschi, A.;Böge, M.;Calvi, M.;Cancellieri, C.;Casati, N.;Cervellino, A.;Chen, Q.;David, C.;Flechsig, U.;Gozzo, F.;Henrich, B.;Jäggi-Spielmann, S.;Jakob, B.;Kalichava, I.;Karvinen, P.;Krempasky, J.;Lüdeke, A.;Lüscher, R.;Maag, S.;Quitmann, C.;Reinle-Schmitt, M. L.;Schmidt, T.;Schmitt, B.;Streun, A.;Vartiainen, I.;Vitins, M.;Wang, X.;Wullschleger, R. The Materials Science Beamline Upgrade at the Swiss Light Source. *J. Synchrotron Radiat.* **2013**, *20*, 667–682.

(28) Dorogokupets, P. I.;Dewaele, A. Equations of State of MgO, Au, Pt, NaCl-B1, and NaCl-B2: Internally Consistent High-Temperature Pressure Scales. *High Press. Res.* **2007**, *27*, 431–446.

(29) Coelho, A. A. TOPAS and TOPAS-Academic: An Optimization Program Integrating Computer Algebra and Crystallographic Objects Written in C Plus. *J. Appl. Crystallogr.* **2018**, *51*, 210–218.

(30) Kresse, G.;Hafner, J. *Ab Initio* Molecular Dynamics for Open-Shell Transition Metals. *Phys. Rev. B* **1993**, *48*, 13115–13118.

(31) Kresse, G.;Furthmüller, J. Efficiency of Ab-Initio Total Energy Calculations for Metals and Semiconductors Using a Plane-Wave Basis Set. *Comput. Mater. Sci.* **1996**, *6*, 15–50.
(32) Kresse, G.;Furthmüller, J. Efficient Iterative Schemes for *Ab Initio* Total-Energy Calculations Using a Plane-Wave Basis Set. *Phys. Rev. B* **1996**, *54*, 11169–11186.
(33) Kresse, G.;Joubert, D. From Ultrasoft Pseudopotentials to the Projector Augmented-Wave Method. *Phys. Rev. B* **1999**, *59*, 1758–1775.
(34) Perdew, J. P.;Burke, K.;Ernzerhof, M. Generalized Gradient Approximation Made Simple. *Phys. Rev. Lett.* **1996**, *77*, 3865–3868.
(35) Grimme, S. Semiempirical GGA-type density functional constructed with a long-range dispersion correction. *J. Comput. Chem.* **2006**, *27*, 1787–1799.
(36) Nazarian, D.;Ganesh, P.;Sholl, D. S. Benchmarking Density Functional Theory Predictions of Framework Structures and Properties in a Chemically Diverse Test Set of Metal–Organic Frameworks. *J. Mater. Chem. A* **2015**, *3*, 22432–22440.
(37) Methfessel, M.;Paxton, A. T. High-Precision Sampling for Brillouin-Zone Integration in Metals. *Phys. Rev. B* **1989**, *40*, 3616–3621.
(38) Fisch, M.;Lanza, A.;Boldyreva, E.;Macchi, P.;Casati, N. Kinetic Control of High-Pressure Solid-State Phase Transitions: A Case Study on l-Serine. *J. Phys. Chem. C* **2015**, *119*, 18611–18617.
(39) Bennett, T. D.;Keen, D. A.;Tan, J.-C.;Barney, E. R.;Goodwin, A. L.;Cheetham, A. K. Thermal Amorphization of Zeolitic Imidazolate Frameworks. *Angew. Chemie Int. Ed.* **2011**, *50*, 3067–3071.
(40) Widmer, R. N.;Lampronti, G. I.;Anzellini, S.;Gaillac, R.;Farsang, S.;Zhou, C.;Belenguer, A. M.;Wilson, C. W.;Palmer, H.;Kleppe, A. K.;Wharmby, M. T.;Yu, X.;Cohen, S. M.;Telfer, S. G.;Redfern, S. A. T.;Coudert, F.-X.;MacLeod, S. G.;Bennett, T. D. Pressure Promoted Low-Temperature Melting of Metal–Organic Frameworks. *Nat. Mater.* **2019**, *18*, 370–376.
(41) Lehnert, R.;Seel, F. Darstellung Und Kristallstruktur Des Mangan(II)- Und Zink(II)-Derivates Des Imidazols. *Zeitschrift für Anorg. und Allg. Chemie* **1980**, *464*, 187–194.
(42) Spencer, E. C.;Angel, R. J.;Ross, N. L.;Hanson, B. E.;Howard, J. A. K. Pressure-Induced Cooperative Bond Rearrangement in a Zinc Imidazolate Framework: A High-Pressure Single-Crystal X-Ray Diffraction Study. *J. Am. Chem. Soc.* **2009**, *131*, 4022–4026.
(43) Masciocchi, N.;Attilio Ardizzoia, G.;Brenna, S.;Castelli, F.;Galli, S.;Maspero, A.;Sironi, A. Synthesis and Ab-Initio XRPD Structure of Group 12 Imidazolato Polymers. *Chem. Commun.* **2003**, *0*, 2018–2019.
(44) Baburin, I. A.;Leoni, S. Modelling Polymorphs of Metal-Organic Frameworks: A Systematic Study of Diamondoid Zinc Imidazolates. *CrystEngComm* **2010**, *12*, 2809–2816.
(45) Gonzalez-Platas, J.;Alvaro, M.;Nestola, F.;Angel, R. EosFit7-GUI: A New Graphical User Interface for Equation of State Calculations, Analyses and Teaching. *J. Appl. Crystallogr.* **2016**, *49*, 1377–1382.
(46) Putnis, A. *An Introduction to Mineral Sciences*; Cambridge University Press: Cambridge, 1992.
(47) Klotz, S.;Chervin, J. C.;Munsch, P.;Marchand, G. Le. Hydrostatic Limits of 11 Pressure Transmitting Media. *J. Phys. D. Appl. Phys.* **2009**, *42*, 75413.
(48) Greaves, G. N.;Sen, S. Inorganic Glasses, Glass-Forming Liquids and Amorphizing Solids. *Adv. Phys.* **2007**, *56*, 1–166.
(49) Machon, D.;Dmitriev, V. P.;Bouvier, P.;Timonin, P. N.;Shirokov, V. B.;Weber, H.-P. Pseudoamorphization of Cs_2HgBr_4. *Phys. Rev. B* **2003**, *68*, 144104.

(50) Navrotsky, A. Nanoscale Effects on Thermodynamics and Phase Equilibria in Oxide Systems. *ChemPhysChem* **2011**, *12*, 2207–2215.
(51) Zhang, C.;Gee, J. A.;Sholl, D. S.;Lively, R. P. Crystal-Size-Dependent Structural Transitions in Nanoporous Crystals: Adsorption-Induced Transitions in ZIF-8. *J. Phys. Chem. C* **2014**, *118*, 20727–20733.
(52) Belenguer, A. M.;Lampronti, G. I.;Cruz-Cabeza, A. J.;Hunter, C. A.;Sanders, J. K. M. Solvation and Surface Effects on Polymorph Stabilities at the Nanoscale. *Chem. Sci.* **2016**, *7*, 6617–6627.
(53) Horike, S.;Shimomura, S.;Kitagawa, S. Soft Porous Crystals. *Nat. Chem.* **2009**, *1*, 695–704.

TOC